A Connected Array of Coherent Photoconductive Pulsed Sources to Generate mW Average Power in the Submillimeter Wavelength Band

Alessandro Garufo [ID], *Member, IEEE*, Paolo Maria Sberna, Giorgio Carluccio [ID], *Member, IEEE*, Joshua R. Freeman, David R. Bacon, Lianhe Li, Juan Bueno, Jochem J. A. Baselmans [ID], Edmund H. Linfield, Alexander G. Davies, Nuria Llombart [ID], *Senior Member, IEEE*, and Andrea Neto [ID], *Fellow, IEEE*

Abstract—A pulsed photoconductive terahertz (THz) source is presented that is able to radiate milliwatt (mW) level average power over a large bandwidth, by exploiting both the optical and electrical properties of photoconductive sources and the ultrawideband properties of connected antenna arrays. An optical system composed of a microlenses array splits the laser beam into $N \times N$ spots that host the active excitation of the antenna arrays. An "ad hoc" network is introduced to bias the array active spots in order to implement a connected antenna array configuration. The array feeds a silicon lens to increase the directivity of the radiated THz beam. A dipole and a slot array are designed. Prototypes have been fabricated and measured. Power and spectrum measurements of the prototypes are in excellent agreement with the expected results. The proposed solutions achieve excellent power radiation levels by exploiting accurate electromagnetic design. Thus, they can offer enhancements to any active system relying on pulsed photoconductive antennas.

Index Terms—Connected arrays, photoconductivity, terahertz (THz) photoconductive antennas (PCAs), THz radiated power, THz sources, THz technology, THz time-domain measurements, ultrawideband arrays.

A. Garufo was with the Microelectronics Department of the Electrical Engineering, Mathematics and Computer Science Faculty, Delft University of Technology, Delft 2628 CD, The Netherlands. He is now with the Radar Technology Department, TNO Defence, Security, and Safety, The Hague 2597 AK, The Netherlands (e-mail: alessandro.garufo@tno.nl).

P. M. Sberna, N. Llombart, and A. Neto are with the Microelectronics Department of the Electrical Engineering, Mathematics and Computer Science Faculty, Delft University of Technology, Delft 2628 CD, The Netherlands (e-mail: p.m.sberna@tudelft.nl; n.llombartjuan@tudelft.nl; a.neto@tudelft.nl).

G. Carluccio was with the Microelectronics Department of the Electrical Engineering, Mathematics and Computer Science Faculty, Delft University of Technology, Delft 2628 CD, The Netherlands. He is now with NXP Semiconductors, High Tech Campus 46, Eindhoven 5656 AE, The Netherlands (e-mail: g.carluccio@tudelft.nl).

J. R. Freeman, D. R. Bacon, L. Li, E. H. Linfield, and A. G. Davies are with the Institute of Microwaves and Photonics of the School of Electronic and Electrical Engineering, University of Leeds, Leeds LS29JT, U.K. (e-mail: j.r.freeman@leeds.ac.uk; d.r.bacon@leeds.ac.uk; l.h.li@leeds.ac.uk; e.h.linfield@leeds.ac.uk; g.davies@leeds.ac.uk).

J. Bueno and J. J. A. Baselmans are with the Netherlands Institute of Space Research (SRON), Utrecht 3584 CA, The Netherlands (e-mail: j.bueno@sron.nl; j.baselmans@sron.nl).

Color versions of one or more of the figures in this paper are available online at http://ieeexplore.ieee.org.

Digital Object Identifier 10.1109/TTHZ.2019.2896791

I. INTRODUCTION

THE emergence of a large variety of applications, for terahertz (THz) technology in recent years [1]–[13], has been driven by the availability of photoconductive antennas (PCAs) that have provided power up to THz frequencies at a relatively low cost, [1]–[3], [14]–[17], thanks to several breakthroughs in photonics, and semiconductor technology [18]–[24]. PCAs are a combination of THz antennas and semiconductor materials driven by optical laser sources that exploit photoconductivity to radiate power over large bandwidths, reaching THz frequencies. Currently, the power radiated by these devices is limited by the high dispersivity and poor radiation efficiency of the existing PCA designs [25]. These bottlenecks render the integration time to detect the THz signal longer than really necessary and, as a consequence, these devices are limited to short-range applications (e.g., spectroscopy). Alternative solutions for radiating high-level power in the submillimeter band have been developed in the last decades [26]. In particular, hundredths of milliwatt (mW) have been recently obtained resorting to frequency multipliers in conjunction with microwave sources [27]. However, these are tunable continuous wave solutions, which do not generate broadband pulses.

The maximum power emitted by a single PCA is limited by the maximum value of biasing voltage applied to the material, which can lead to the failure of the substrate material if it exceeds the voltage breakdown, and the maximum laser power that can cause a thermal failure of the device. Moreover, even before failure, large amounts of laser power and/or a high bias voltage lead to the saturation of the photocurrent [28]–[30], limiting the available power of the device. In order to increase the available radiated THz power, various PCA array structures have been proposed in the recent years [31]–[40]. However, all these technological solutions are electromagnetically inefficient when they operate over wide bandwidths in a pulsed system. This is because they all rely on array arrangements of electrically short radiating elements [41].

In this paper, we describe the design and analysis of a connected array of photoconductive sources (PCCA), which was presented for the first time in [42]. A PCCA can be viewed as a modification of a connected array antenna [43]–[49], which is characterized by an intrinsic wideband radiation performance.
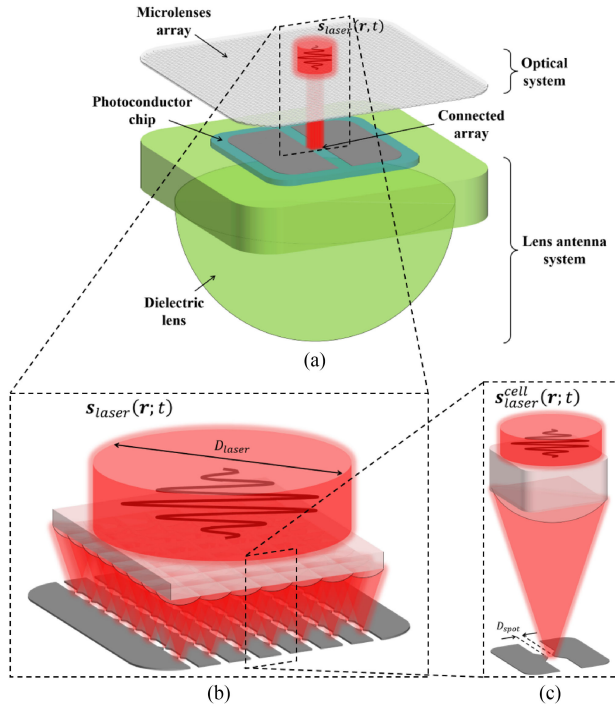
Fig. 1. Structure of the photoconductive connected array: (a) general view of the system structure. (b) View of the connected array and its excitation optical network. (c) View of the cell excitation.
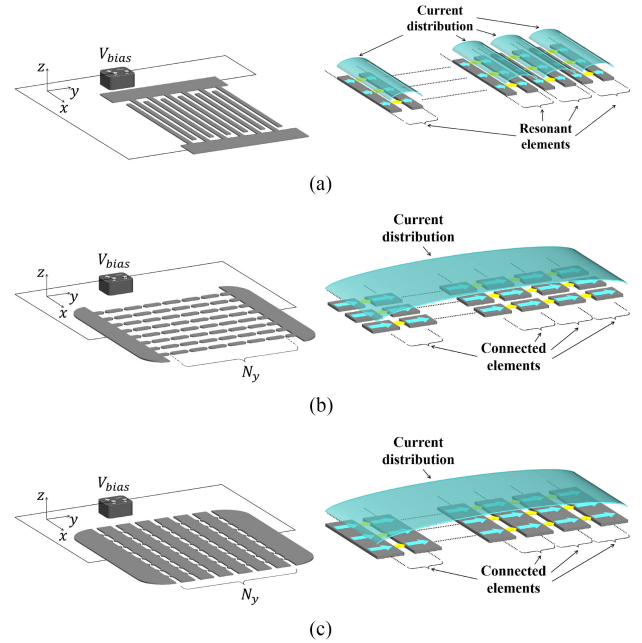

Fig. 2. Biasing networks and relevant current distributions of photoconductive interdigitated array and connected array: (a) interdigitated based structure, (b) dipole based connected structure, and (c) slot based connected structure. The yellow arrows represent the impressed currents at multiple periodic locations, the light blue arrows represent the induced current on the array elements. The shaded light blue surfaces depict the current amplitude distribution on the array structures.

This property makes connected array of sources suitable to efficiently radiate the wideband pulses generated in the optically pumped photoconductive gaps [41]. The designs, presented in this paper, target at large submillimiter (mm) wavelength bandwidth (the measured energy spectrum covers a bandwidth at −5 dB from 0.1 to 0.6 THz). In this bandwidth the proposed solution presents clean radiation patterns and high radiation efficiency.

The paper is structured as follows. Section II discusses the implementation of the connected array structure for PCAs. Section III describes the design, the manufacturing, and the assembling processes of the array prototypes. Section IV describes the measurement setup used for the characterization of the prototypes. Section V is dedicated to the electromagnetic (EM) dispersion analysis and the power budget of the proposed PCCA designs and the quasi-optical (QO) system of the measurement setup. Section VI presents the power and energy spectral density measurement of the prototypes, and the relevant comparisons against the theoretical results. Finally, Section VII discusses some concluding remarks. Additionally, Appendix A presents the procedure used to estimate the focusing performance of the optical system of the PCCA. Appendix B summarizes the method for evaluating the energy spectral density generated by the photoconductive array.

II. ARCHITECTURE OF A PCCA-BASED SOURCE

The proposed photo-source architecture is shown in Fig. 1(a). The design of a pulsed PCCA source involves two components: the connected array that includes the biasing network; and the optical system used to excite the photoconductive gaps of the array cells [see Fig. 1(b) and (c)]. The optical system consists of a microlenses array, which splits the laser beam, and focuses a portion of the beam on each gap of the array. The connected array structure has two functions: biasing and wideband radiation at THz frequencies. For the biasing function, it uses a connected biasing network that feeds the gaps in series, providing the bias voltage at each array cell to accelerate the free carriers excited by the optical pulses absorbed in the semiconductor. At THz frequencies, the connected array radiates the EM energy associated to these transient electric currents. The array is coupled to a dielectric silicon lens to increase the antenna directivity of the THz radiation. In the following sections each component of the antenna system will be discussed.

A. Biasing Network

Typically, a photoconductive array uses an interdigitated structure for implementing the biasing network of the array [see Fig. 2(a)]. Indeed, this arrangement is encountered in [31]–[33], and [50], where the authors used the interdigitated electrode structure over a large photoconductive area. The structure effectively realized an array of dipoles. However, when the interdigitated fingers of the electrodes are biased, the electric field direction between successive fingers is opposite and, when illuminated, the biasing induces dipoles with opposite orientations between them. Consequently, the fields radiated by opposite dipoles cancel each other in the array antenna far-field region. In order to avoid such a destructive interference, a second metallization (mask), which is electrically insulated from that of the electrodes, is used. This prevents the excitation of the

photoconductive material between two consecutive fingers and leads to a distribution of dipoles, which are oriented in the same direction on all the array surface [see Fig. 2(a)]. An alternative solution adopted in [34], [37], and [38] is to etch away the photoconductive material in the alternating regions. Both these solutions have the drawback that not all the optical power is used in exciting the photoconductive array; part is reflected by the masking metallizations or it does not excite free charges in the regions where the photoconductor is removed. To mitigate this problem, an array of microlenses can be used to only illuminate alternate gaps between the biasing fingers [35]. With this method, the laser power is focused for exciting the photoconductor material and a unidirectional dipoles excitation is induced without the necessity of any additional masking layer or photoconductor removal. More recently, in [40], the authors proposed an array solution similar to the large interdigitated array in [32] with the masking metallizations. However, in order to have a higher transmitted electric field in the photoconductive material, they suitably shaped one of the electrodes by introducing periodic thin metallizations. By such shaping, a higher absorption of the optical power is obtained.

In this paper, a different "ad hoc" biasing scheme is introduced to implement the photoconductive coherent source, with the aim of using effectively the whole laser energy that impinges on the array area, and to implement a connected array structure. The biasing networks for both dipole- and slot-based array are shown in Fig. 2(b) and (c). The bias voltage V_{bias} is applied at the edges of the array. Adjacent gap metallizations behave as capacitors connected in series, and they are charged by the applied bias. Since the array structure is symmetric, and the cells are identical, the bias voltage V_{bias} is equally divided among all the rows of elementary cells $V_{\text{bias}}^{\text{cell}} = V_{\text{bias}}/N_y$ [see Fig. 2(b) and (c)]. Each of the gaps experiences biasing electric fields in the same direction. In the presence of the laser illumination the capacitances are discharged, by the generated free carriers that are accelerated, forming a current from the cathode to the anode. In the ideal scenario of a uniform illumination, the bias voltage is equally divided among the gaps. In the real case, where a Gaussian tapering of the laser illumination can be assumed, we implemented a moderate −3 dB tapering at the array edges, which does not lead to a significant inhomogeneous bias voltage variation, approximating the ideal case. Therefore, according to the gaps position on the array, the gaps experience a slightly different voltage drop, due to the different laser excitation on the array cells. The voltage has the same time-varying behavior for all the gaps except for the amplitude, which depends on the gap position with respect to the laser excitation profile. This effect is clearly localized on the gaps. However, the carriers acceleration induces a global propagation of EM field in the surrounding of the array cells metallization. This field induces pulsed currents on the metallization, which are responsible of the THz radiation. This current flowing on the array structure is continuous across the array cells, as in Fig. 2(b) and (c), without the presence of discontinuities, and its distribution follows the impinging laser beam profile, which can be considered almost uniform, when the array area is illuminated with a laser profile, which presents a −3 dB power level at the array edges. This effectively realizes a connected array. One should keep in mind that this description is valid in the time frame in which the photoconductive sources are active, due to the laser illumination. As soon as the illumination is removed (after the laser pulse) and the free carriers recombine, the array cannot be treated as connected. This state should not influence the pulsed radiation performance since all the available power should be radiated when the gaps are active.

B. Radiation via a Connected Array

The connected arrays in Fig. 2(b) and (c) are arrays of radiating elements that are fed by currents impressed at multiple periodic locations. The feeding terminals are connected in series and they can be viewed as generating a unique total current distribution over the entire array [43]–[49], as it is shown in Fig. 2(b) and (c). End points induced resonances, which normally are associated to short dipoles [see Fig. 2(a)], will not occur for connected arrays. The uniform current distribution radiates a short pulse directly in the lens. The limiting factor for the upper limit of the bandwidth is then the appearance of grating lobes in the beam associated with higher frequencies, when the periodicity of the radiating elements is equal or greater than half-wavelength $d_x = d_y \geq \lambda_r/2$, with $\lambda_r = \lambda_0/\sqrt{\varepsilon_r}$, where λ_0 is the free-space wavelength and ε_r is the relative dielectric constant of the lens material. The limiting factor for the lower limit of the bandwidth of a connected array is the edge truncation effects, introduced by the finite electrical dimensions of the array. It was also shown that connected arrays can be used to efficiently illuminate the surface of dielectric lens antennas over a large bandwidth [47]–[49]. The proposed system is therefore suitable for radiating pulsed EM energy with a wideband spectrum, as the one generated in optically pumped semiconductor materials (e.g., LT-GaAs or LT-InGaAs).

C. Optical Excitation System

The present connected arrays can be designed such that each of the feeding gaps will present an active impedance comparable to the wave impedance of the dielectric of the lens $\zeta_d \approx 110\,\Omega$. Accordingly, in order to obtain matching between the active impedances and the source impedances, the latter would also have to be on the order of $100\,\Omega$. As explained in [51], the average impedance of the source can be fine-tuned to such low values by focusing the laser beams onto very small gaps. The ideal matching could be reached by properly sizing and optically exciting the array cells gaps. For this purpose, an array of microlenses has to be employed, as in [35], [36], and [52]. The microlenses array splits and focuses the laser beam, illuminating the whole array area, into the array feeding gaps, as shown in Fig. 1(b). Moreover, in order to have a uniform current distribution on the array [see Fig. 2(b) and (c)], the laser beam spatial distribution has to be uniform.

III. DESIGN OF PCCA-BASED SOURCE FOR SUB-MM RADIATION

In this section, we present the design and the manufacturing of two connected array photoconductive sources structures, that radiate in the sub-mm bandwidth (<1 THz).
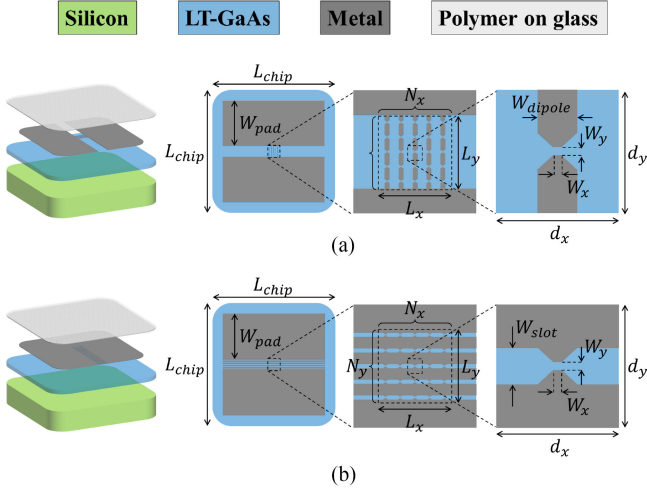
Fig. 3. Structures of the PCCA designs. The blue slab represents the photoconductive material chip; the green thick slab depicts the silicon lens; the array metallizations are depicted in grey; whereas the microlenses array is represented by the light gray slab. (a) Dipole-based structure. (b) Slot-based structure. The arrays are composed by $N_x = N_y = 5$ square cells, cells size $d_x = d_y = 100\,\mu$m, array length $L_x = L_y = 0.5$ mm, bias pad width $W_{\mathrm{pad}} = 2.25$ mm, and overall chip dimension $L_{\mathrm{chip}} = 6$ mm. Dipole width $W_{\mathrm{dipole}} = 20\,\mu$m, slot width $W_{\mathrm{slot}} = 30\,\mu$m, and gap size $W_x = W_y = 7.5\,\mu$m.
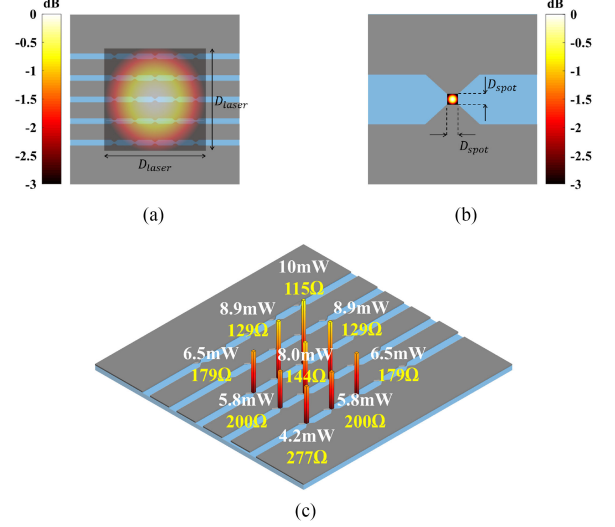

Fig. 4. Laser power excitation of the array. (a) Normalized laser beam distribution on the array area before the focusing of the microlenses' array. (b) Normalized laser beam distribution focused by the microlenses' array on each cell gap. (c) Laser power excitation (white text) and relevant generator impedances (yellow text) on the gaps of the array cells, assuming the maximum available laser power. Because of the spatial symmetry of the laser beam only a quarter of the array excitation is shown, in the picture the slot based array is depicted. The same laser excitation is applied to the dipole-based design.

A. Array Design

The design of the arrays was carried out taking into account the spectral energy distribution of the current pulse generated in the photoconductor, resorting to the linear equivalent model for pulsed photoconductive source, developed in [51] and [53] for small bias voltages and laser excitation, where no saturation and screening effects are considered. As it was shown in [51] and [53], for photoconductive sources most of the energy is contained at lower frequencies of the spectrum (<1 THz). The features of the laser available for this design are the following: maximum laser average power $\bar{P}_{\mathrm{laser}}^{\mathrm{max}} = 0.5$ W, carrier frequency $f_{\mathrm{laser}} = 375$ THz (central wavelength $\lambda_{\mathrm{laser}} = 800$ nm), pulse duration $\tau_p = 100$ fs, and a repetition rate frequency $f_p = 80$ MHz.

The laser beam has to be split and focused by an array of microlenses in order to illuminate the feeding array gaps. Referring to Fig. 3, the spatial periodicity of the PCCA cells has to be equal to the periodicity of the microlenses array. Such periodicity dictates the upper limit of the PCCA operative bandwidth because of the grating lobes that arise at higher frequencies. A reasonable small number of array elements for which one can assume that the behavior of each cell of a connected array resembles the behavior of the infinite array structure, i.e., active impedance of $110\,\Omega$, is $5 \times 5 = 25$. The available optical power $\bar{P}_{\mathrm{laser}}$ will not be entirely focused on the gaps, due to the Gaussian power distributions typically produced by lasers. Accordingly, aiming at a quite uniform excitation of the array, a 3 dB loss of optical power has to be taken into account in the design, due to the spillover onto the array area, see Fig. 4(a). Moreover, a further 3 dB loss of the optical power associated with the spillover on each gap has to be taken into account in order to approximate a uniform illumination of the gaps, see Fig. 4(b). Therefore,

assuming a laser beam with diameter at -3 dB equal to the size of the array, $D_{\mathrm{laser}}^{\mathrm{ideal}} = L_x = L_y$, total optical transmission of the microlenses, and the laser spot focused by the microlenses at -3 dB matched to the gaps width $D_{\mathrm{spot}}^{\mathrm{ideal}} = W_x = W_y$, the optical power incident on each cells gap can be evaluated. By considering the maximum available laser power ($\bar{P}_{\mathrm{laser}}^{\mathrm{max}} = 0.5$ W), ideally the central gap of size $5\,\mu$m $\times$ $5\,\mu$m of the array would be excited by 10 mW of optical power, see Fig. 4(c), that would guarantee a source impedances of roughly $115\,\Omega$, considering a carriers lifetime $\tau = 0.3$ ps and a transient carriers mobility $\mu = 240$ cm^2/Vs, [51], [53].

A microlenses array with a pitch of $p = 100\,\mu$m [54], the smallest commercially available at the time of the design, which presents a square rim with a 100% fill factor, and a lens focal number $f_\# = 9.5$, has been used in this design. The microlenses array is made of polymer-on-glass [54], which ensures 96% of optical power transmission at wavelengths around 800 nm. The overall dimensions of the array (0.5 mm $\times$ 0.5 mm) determine the lower limit of the operative bandwidth of the array, 0.1 THz. The f-number and the size of the microlenses give a focal distance $f = 0.95$ mm, and a theoretical focused spot size at -3 dB $D_{\mathrm{spot}} = 1.02 f_\# \lambda = 7.75\,\mu$m [55]. The gap sizes of the cells of the arrays have been fixed to ideally match the -3 dB spot size of the laser sub-beams focused by the microlenses, as in Fig. 4(b), $W_x = W_y \approx D_{\mathrm{spot}}$, i.e., $W_x = W_y = 7.5\,\mu$m. As a consequence of the practical optical power distribution, the desired $110\,\Omega$ source impedance could not be achieved. Instead, one could expect the actual average impedance to be $Z_g = 272\,\Omega$ for the central array source. All the geometrical details of the array and its cells are listed in the caption of Fig. 3.
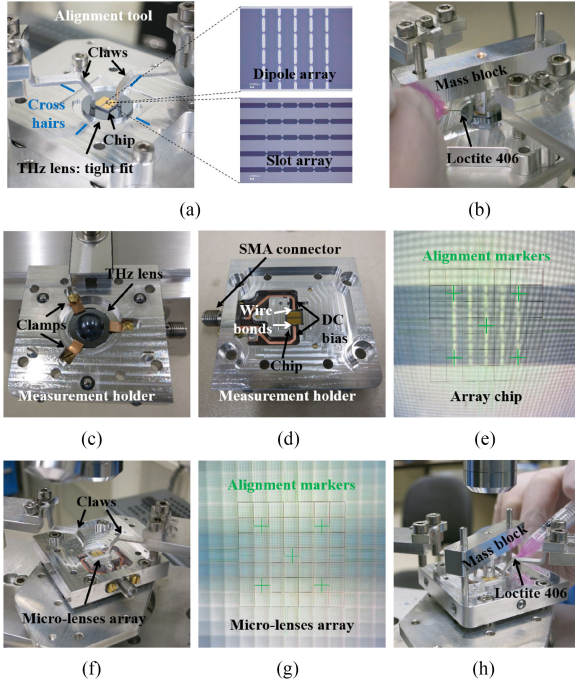
Fig. 5. Assembly procedure. (a) THz lens and array chip mounted into the auxiliary alignment tool. (b) Mass block placed on top of the chip during the glueing to prevent the creation of an air gap between the THz lens and the array chip. (c) Front view of the experiment holder with the THz lens and array chip assembly mounted in it. This assembly in kept in place with three clamps. (d) Back view of the experiment holder with the THz lens and array chip assembly mounted in it. The dc bias lines are connected to the chip with wire bonds. (e) Microscope on-screen markers for the center and the four corners gap elements of the array. (f) Alignment of the microlenses array with the antenna array. (g) Microscope on-screen markers to align the microlenses array with the antenna array. (h) Mass block placed on top of the microlenses array during the glueing to assure that no glue goes under the microlenses array.

Both arrays have been lithographically defined on the same semiconductor wafer, composed of a 2 μm thick annealed LT-GaAs layer [24], grown on a 400 nm thick AlGaAs layer with 0.75% of Al content; itself grown on a GaAs buffer layer of thickness 200 nm placed on a 525 μm thick SI-GaAs wafer. Microscope pictures of the metallization, obtained by photolithography, are shown in the inset of Fig. 5(a). The relative permittivity of the layered semiconductor is about $\varepsilon_{\text{GaAs}} = 13$. For increasing the directivity of the array, a silicon lens [56], with relative permittivity $\varepsilon_{\text{Si}} = 11.9$, has been used with radius $R_{\text{lens}} = 5$ mm, and extension length $E_{\text{lens}} = 0.18R_{\text{lens}}$, in order to get an overall extension length, including the thickness of the chip, equal to the ideal hyperhemispherical extension of the lens $0.29R_{\text{lens}}$, that ensures a more frequency stable pattern. A quarter-wavelength matching layer on the silicon lens at central frequency 0.4 THz has been applied, in order to reduce the reflection at the lens-air interface. Such matching layer has been realized by a 114 μm high-purity parylene coating [57] with relative permittivity $\varepsilon_c = 2.72$.

B. Array Manufacturing

To create the 3-D structure required for the operation of the PCCA, we use an assembly of three different components: the array of optical microlenses, the antenna array chip, and the large

THz lens, shown in Fig. 1. The array of optical microlenses is placed at a distance of 0.95 mm from the antenna array to match the microlenses' focal length. The large THz lens, with a 15 mm rim diameter, is made from high resistivity 2.4×10^5 Ωcm, silicon rod [58], using single point diamond turning [56]. It is placed on the opposite side of the antenna array chip to focus the emerging THz radiation to the detecting element in the experiment (either a power meter or a bolometer). The assembly of these three components is done as follows. First, the large THz lens is mounted into a tool specifically designed for this purpose and built in-house. This alignment tool is an aluminum block in which the THz lens fits tightly (15 μm). The alignment tool has cross hairs engraved with a laser [59], marking the center of the aperture in which the lens is placed. The antenna array chip is placed on top of the flat surface of the THz lens. Using the cross hairs and an optical microscope, the antenna array chip is placed at the center of the lens using two "claws" to hold the chip from the corners [see Fig. 5(a)]. Once the chip is placed at the center of the lens, the THz lens is glued by applying Loctite 406 glue to one of the corners of the array. A mass block is placed on top of the chip during the glueing to minimize the glue gap between the THz lens and the chip [see Fig. 5(b)]. An alignment accuracy better than 10 μm is obtained using this method. Second, the assembly of the THz lens and the chip is removed from the auxiliary alignment tool and mounted and clamped into the holder that will be used in the experiments. The experiment holder also has a tight fit for the THz lens, assuring that the position of the center of the THz lens (and the antenna array) is known. The front and the back of the experiment holder with the THz lens and antenna array chip mounted can be seen in Fig. 5(c) and (e), respectively. The dc bias lines of the PCCA are connected to the printed circuit board (PCB) of the experiment holder with several wire bonds [see Fig. 5(d)]. The dc bias lines of the PCB are connected to an SMA connector to provide the bias voltage to the device. Third, the sample holder is placed under a microscope, which has on-screen markers for the center and the four corners gap elements of the array. The antenna array is aligned with the markers, and its position is fixed for the rest of the alignment [see Fig. 5(e)], with an accuracy of 10 μm. The microlenses array is placed on a specially machined edge of the sample holder, assuring that the distance between the microlenses array and the array gaps is equal to the focal length of the microlenses array. The accuracy of the mechanical machining ensures that this distance is within ± 40 μm, which is within the range of the depth of focus of the microlenses [55]. The same "claws" used previously are now used to move the microlenses array and align it with the antenna array [see Fig. 5(f)]. The outer edges of the lenses of the microlenses array are aligned with the on-screen markers [see Fig. 5(g)]. This alignment has an accuracy of 10 μm. Note that the crosses are used for the array elements and the squares are used for the microlenses array. To finalize the assembly, the microlenses array is glued to the extrusion of the holder with Loctite 406 glue on one of the corners of the array. A similar mass block to the one used in the previous glueing is placed on top of the microlenses array to prevent the creation of a glue gap [see Fig. 5(h)]. This assembly method gives a total alignment accuracy between the THz lens and the microlenses array better than 30 μm. During the experiment, the effects of these
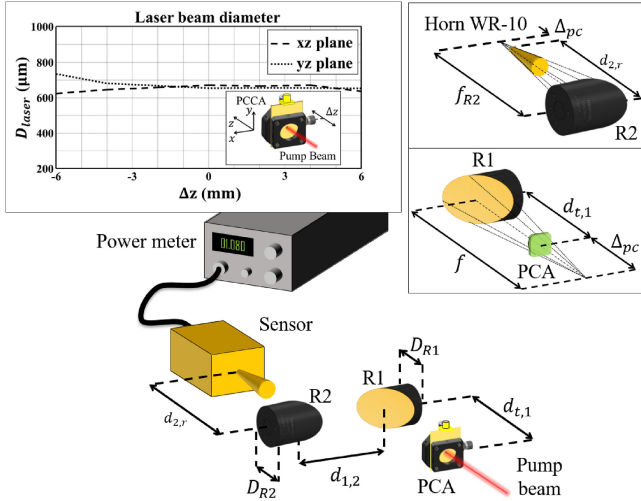
Fig. 6. Measurement setup used to measure the power radiated by the PCA prototypes, the optical system is not depicted in the figures. The geometrical features of the setup are: reflectors diameter $D_{R1} = D_{R2} = 76.2$ mm: reflectors f-number $f_{\#1} = f_{\#2} = 2$; distance emitter-first reflector $d_{t,1} = 142.4$ mm; distance reflectors $d_{1,2} = 335$ mm; distance second reflector-horn antenna was $d_{2,r} = 142.4$ mm. The top left inset shows the measured laser beam diameter at -3 dB, D_{laser}, along the horizontal (dashed line) and vertical (dotted line) planes around the position of the photoconductive source.

possible misalignments are compensated by using the motorized translational and rotational stage discussed in the following section.

IV. MEASUREMENTS SETUP

The characterization of the PCCA prototypes has been carried out by measuring the radiated power and spectrum.

The measurement setup was composed of two $90°$ off-axis parabolic reflectors and the features of the system are listed in the caption of Fig. 6. For the spectrum measurements, the power meter has been replaced by an electro-optic (EO) crystal system for the detection of the THz pulses. The position of the emitter with respect to the first reflector has been chosen in such a way to match the phase center of the hyperhemispherical lens antenna, placed 10 mm (Δ_{pc}) behind the antenna plane, with the focal point of the parabolic reflector, $d_{t,1} = f_{R1} - \Delta_{pc} = 142.4$ mm.

The features of the laser used for the experiment are the ones discussed in Section III-A. The laser excitation $\mathbf{s}_{\text{laser}}(\mathbf{r}; t)$ was focused on the antenna array by means of an optical path, which included a telescopic lens system, composed by a concave and a convex lens, chosen to match the area of the antenna array, as discussed in Section III-A. The top left inset of Fig. 6 shows the laser beam diameter at -3 dB measured on both horizontal and vertical planes by means of the knife-edge technique on a longitudinal range centered around the position of the photoconductive source in the measurement setup $d_{t,1}$. The average laser beam diameter obtained by such telescopic lens system was $D_{\text{laser}} = 660\,\mu$m, larger than the ideal scenario discussed in Section III-A, $D_{\text{laser}}^{\text{ideal}} = 500\,\mu$m. The knife-edge measurements were carried out by using a motorized translation stage system [60], programmed to perform rasterscan measurements on both

horizontal and vertical planes, which also provided the relative position of the laser beam with respect to the reference system of the translational stage.

After positioning the device in the laser beam, the alignment of the device position was optimized by using the same motorized stage system [60]. The motorized stage was composed of three translation stages, allowing movements along the three space directions (x, y, z), with a resolution of $1.25\,\mu$m movement, and two rotational stages, rotating in the azimuthal and elevation planes, with an angular resolution of $0.01°$. This resolution for the alignment was needed for centering accurately the devices with respect to the laser beam, and for compensating possible misalignment of the focused laser beams with respect to the array gaps, due to any slanting incidence of the laser beam on the microlenses array.

The focusing of the microlenses array has been experimentally estimated to provide a focused spot at -3 dB $D_{\text{spot}} = 10\,\mu$m, as discussed in Appendix A. This laser spot diameter is also larger than the ideal value considered during the design analysis in Section III-A.

V. PCCA ESTIMATED PERFORMANCE

The analysis of the arrays has been carried out following the same procedure discussed in [53]. In detail, the EM analysis of the connected arrays has been performed by using the commercial software [61], assuming the chip structure to radiate between free space and a semi-infinite dense dielectric medium, which simulates the presence of a dielectric silicon lens [25]. The simulated radiation patterns of the arrays in the semi-infinite silicon medium have been used to compute the fields radiated by the dielectric lens via a physical optics (PO) approach [49], [62]. Finally, in order to characterize the measurement setup when it is fed by the PCCA, the EM behavior of the reflectors system has been simulated by means of a PO approach, and the coupling between the beam emerging from the last reflector and the detector has been simulated by a method of moments, both implemented in the commercial software [63].

A. Array Radiation

The array geometries have been simulated weighting the excitation at each port, taking into account the illumination of the gaps provided by the optical system design discussed in Sections III and IV, and loading the ports with the impedances evaluated by using the equivalent circuit in [51].

The simulated active input impedances of the array cells, considering a laser power excitation of 500 mW, for both dipole- and slot-based designs are shown in Fig. 7. The active resistances of the array cells oscillate around the value of the active resistance of the cell in infinite connected array configuration (red dash-dotted line in Fig. 7). This is due to the small number of array elements considered in this design. The dipole array presents active resistances oscillating around $100\,\Omega$ [see Fig. 7(a)], while the values for the slot array center around $50\,\Omega$ in the bandwidth below 0.7 THz [see Fig. 7(b)]. Moreover, the estimated active reactances also show oscillating values, due to the truncation of the structure, but the relevant absolute values are much lower
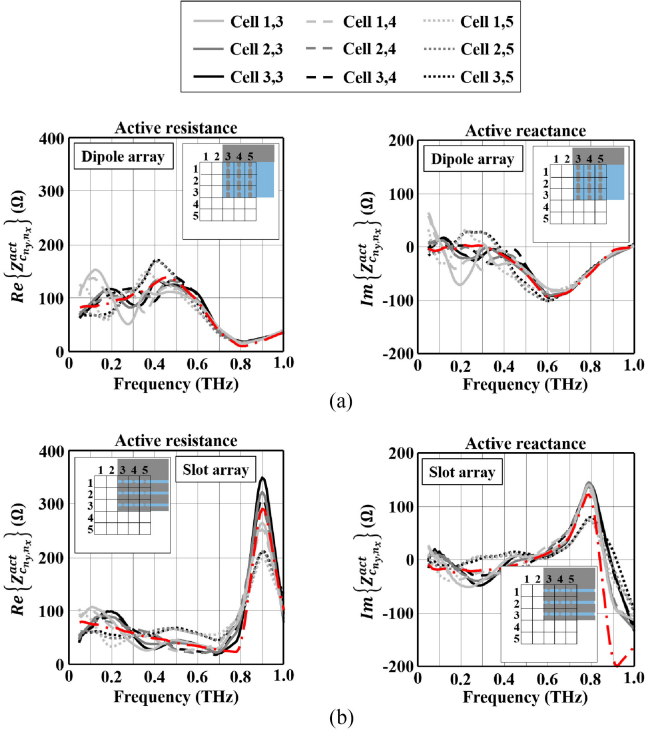
Fig. 7. Active impedance of the array cells. (a) Dipole-based design. (b) Slot-based design. Because of the symmetrical excitation of the array elements, only the active impedances of the cells in a quarter of the arrays are shown. The red dash-dotted lines refer to the active resistances and reactances of the unit cell in an infinite connected array configuration.
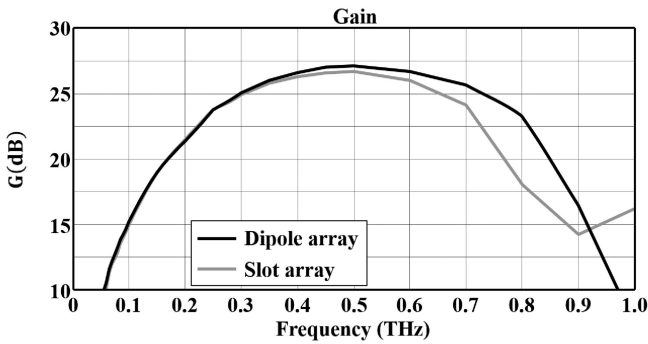

Fig. 8. Simulated gain of the array designs. The evaluation of the gain takes into account the front-to-back losses, the dielectric losses of the silicon, and the reflection losses at the lens interface including the effect of the matching layer.

than the ones of an array constituted by small resonant elements. For frequencies above 0.7 THz, the effects of grating lobes on the active impedances arise. In particular, the active resistances of the dipole array tend to zero, whereas the active resistances of the slot array increase, showing a maximum around 0.9 THz. This is due to the dimensions of the unit cell, which becomes comparable to the effective wavelength, and this results in the out of phase coupling between the ports of adjacent unit cells.

By using the simulated radiation patterns of the arrays inside (Primary Field) and outside (Secondary Field) the dielectric lens, the gain of the array designs has been computed, see Fig. 8. This
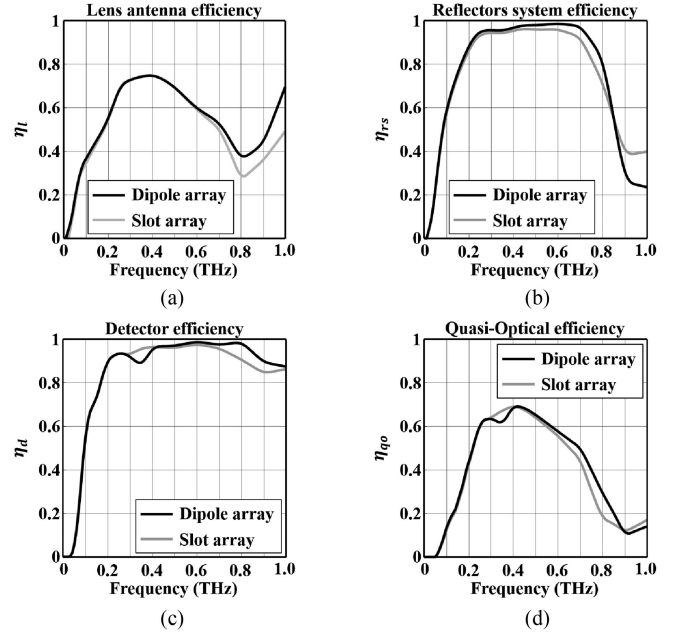

Fig. 9. Simulated efficiencies of the measurement setup. (a) Lens antenna efficiency η_l. (b) Reflectors system efficiency η_{rs}. (c) Detector efficiency η_d. (d) QO efficiency η_{qo} of the measurements setup.

takes into account the front-to-back losses, dielectric losses of the silicon according to [64], and the reflection losses at the lens interface [62] including the effect of the matching layer. These gains do not include the matching efficiency between the active antenna and the source impedances. The array designs present similar performances, in terms of radiation patterns, over the operative bandwidth (< 1 THz).

B. QO System

The characterization of the measurement setup has been performed in terms of efficiency of all stages on the radiated pulsed bandwidth. The entire QO channel, used to couple the radiated energy to the detector, can be characterized by the QO channel efficiency [53]

$$\eta_{qo}(\omega) = \eta_l(\omega)\,\eta_{rs}(\omega)\,\eta_d(\omega) \tag{1}$$

where the lens antenna efficiency η_l takes into account the front-to-back losses, the dielectric losses of the silicon according to [64], and the reflection losses at the lens interface [62], including the matching layer. The ohmic losses in the metallizations have not been considered since they are negligible; the reflectors system efficiency η_{rs} takes into account the spillover losses of the reflectors chain; and the detector efficiency η_d considers the coupling losses between the reflectors system, the conical horn antenna, and the waveguide inside the detector. All these efficiencies are defined and discussed in detail in [53]. For the proposed array designs such efficiencies are shown in Fig. 9. The lens antenna array designs show the highest radiation efficiency η_l around 0.4 THz, because of the presence of the matching layer designed at this frequency. On the contrary, the coupling between the lens antenna arrays and the reflector system η_{rs}

TABLE I
ESTIMATED AND MEASURED AVERAGE POWER OF THE PHOTOCONDUCTIVE CONNECTED ARRAYS

| | $\bar{P}_{laser}$ | V_{bias} | V_{bias}^{cell} | E_{bias}^{cell} | Estimated Power | | | | Measured Power |
					$\bar{P}_{available}$	$\bar{P}_{source}$	$\bar{P}_{lens}$	$\bar{P}_{meas}^{theo}$	
Dipole	500 mW	200 V	40 V	5.33 V/μm	1.76 mW	0.45 mW	0.27 mW	0.21 mW	221 μW
		300 V	60 V	8 V/μm	3.96 mW	1.01 mW	0.60 mW	0.48 mW	448 μW
		400 V	80 V	10.67 V/μm	7.04 mW	1.80 mW	1.07 mW	0.86 mW	712 μW
Slot	500 mW	200 V	40 V	5.33 V/μm	1.76 mW	0.36 mW	0.18 mW	0.13 mW	121 μW
		300 V	60 V	8 V/μm	3.96 mW	0.81 mW	0.41 mW	0.29 mW	334 μW
		400 V	80 V	10.67 V/μm	7.04 mW	1.44 mW	0.73 mW	0.52 mW	475 μW
Bow-tie	100 mW	–	60 V	6 V/μm	0.74 mW	0.39 mW	0.26 mW	0.10 mW	92 μW
		–	80 V	8 V/μm	1.31 mW	0.69 mW	0.45 mW	0.18 mW	158 μW
		–	100 V	10 V/μm	2.05 mW	1.08 mW	0.71 mW	0.28 mW	241 μW

shows a flat behavior around this central operative frequency, with a degradation of the spillover at lower and higher frequencies of the operative bandwidth, because of the lower directivity provided by the lens antenna, due to the arise of grating lobes in the array radiation patterns inside the dielectric lens. The reflectors system fed by the lens array designs present very high and flat coupling efficiency η_d with the detector, due to the high focusing of the beam into the horn antenna of the detector. A poor coupling is shown at the lower frequencies, because of the presence of a WR-10 waveguide in the power meter. Finally, it is worth noting that the efficiencies of all the measurement setup stages have the same behavior for both the array type designs, due to the same radiation performances provided by both lens antenna arrays, as it has been shown in Section V-A. As a result, the QO channel efficiencies η_{qo}, Fig. 9(e), shows almost the same behavior over the entire operative bandwidth for both the designs.

C. Spectrum and Power Budget

The results of the EM analysis of the array and the measurement setup has been used, jointly with the equivalent circuit for pulsed PCAs presented in [51] and [53], to compute the radiated and measured energy spectra and average power of the photoconductive array designs.

The energy spectra E_s radiated by the proposed array designs can be calculated as discussed in Appendix B. Similarly, the energy spectra densities $E_s^{\max}$ of the maximum available energy provided by the photoconductor gaps to an array with matched loads can be calculated, see Appendix B.

Moreover, having the characterization of the lens antenna in terms of efficiency η_l at each frequency, discussed in the previous section, the energy spectrum radiated by the lens E_l can be calculated from the energy spectrum radiated by the photoconductive array E_s as in [53]

$$E_l\left(\omega\right) = \eta_l\left(\omega\right) E_s\left(\omega\right). \tag{2}$$

The estimated energy spectra E_s and E_l radiated by the photoconductive lens antenna arrays are shown in Fig. 10. The results refer to a laser excitation $\bar{P}_{\text{laser}} = 500$ mW, and a bias voltage $V_{\text{bias}} = 200$ V, considering a LT-GaAs with carrier lifetime $\tau = 0.3$ ps, and a transient carrier mobility $\mu = 180$ cm^2/Vs, as it will be discussed in Section VI-A.
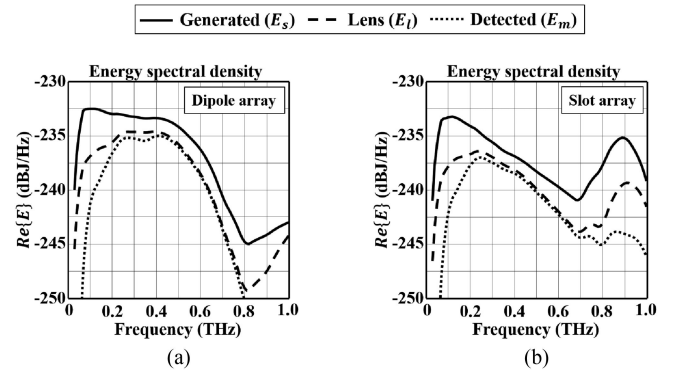

Fig. 10. Simulated energy spectral density of the PCCA: (a) dipole array and (b) slot array, respectively. The plots show the energy spectral densities generated by the arrays E_s (solid lines); the energy spectral densities radiated by the dielectric lens fed by the arrays E_l (dashed line); and the detected energy spectral densities E_m (dotted line).

Since the PCCA radiates periodically with a period $T_p = 1/f_p$, where f_p is the repetition rate of the laser excitation, the average power associated with each spectrum can be calculated by integrating the relevant energy spectral density, and dividing by the laser repetition rate T_p, as in [53], i.e.,

$$\bar{P} = \frac{1}{2\pi T_p} \int_{-\infty}^{+\infty} E\left(\omega\right) d\omega. \tag{3}$$

In particular, from the energy spectral densities $E_s^{\max}$, E_s, and E_l, the average powers $\bar{P}_{\text{available}}$, $\bar{P}_{\text{source}}$, and $\bar{P}_{\text{lens}}$ can be calculated by (3), respectively. Such powers are listed in the sixth, seventh, and eighth column of Table I, respectively, assuming a laser excitation $\bar{P}_{\text{laser}} = 500$ mW and for different bias voltages.

The powers have been evaluated by integrating the relevant energy spectral densities over a bandwidth 0.05 THz − 1 THz. Comparing the sixth and seventh columns, it is evident that the maximum available power $\bar{P}_{\text{available}}$ is higher than the power radiated $\bar{P}_{\text{source}}$ by the array with this laser excitation. This is due to the low impedance matching efficiency between the photoconductive sources and the array cells. In particular, the 26% and 21% of the available power is radiated by the dipole and slot arrays (see Table I). The different performances in terms of radiated power between the dipole and slot arrays occur because of the different behavior of their active impedances, see Fig. 7(a) and (b). The values of the active resistances of the dipole cells
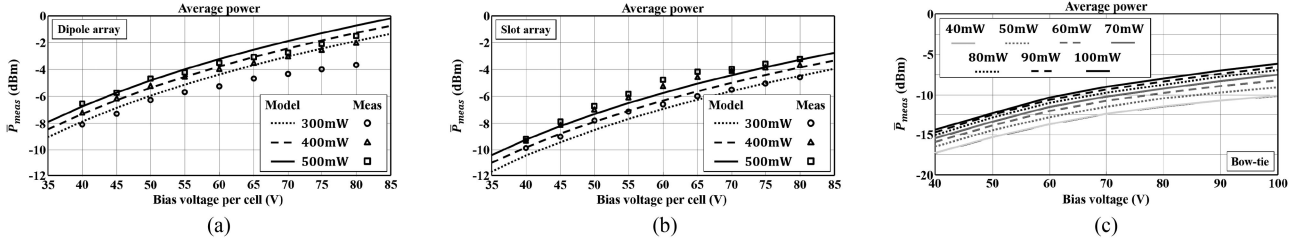
Fig. 11. Measured average power and estimated average detected power $\bar{P}_{\mathrm{meas}}$ of the PCCA prototypes versus the bias voltage applied on the gaps. (a) Dipole array. (b) Slot array. (c) Measured average power of the bow-tie antenna versus bias voltage for different laser power excitations.

are higher than those of the slot cells below 0.7 THz. Above this frequency, the active resistances of the slot array increase, resulting in higher spectral energy density than the dipole array. However, this energy content is lost in the QO channel, since the grating lobes do not properly illuminate the dielectric lens, and consequently the energy does not propagate in the reflectors system, see Fig. 9. Overall, the amount of average power measured for the dipole array results higher than the one measured for the slot array, see Table I.

VI. PCCA MEASURED PERFORMANCE

The power and spectra measurement procedures adopted for the characterization of the PCCA prototypes are discussed in the following section.

A. Power Measurements

The PCCA prototypes were measured by using different values of laser average power and bias voltage. The devices were biased with a voltage square wave with frequency $f_{\mathrm{bias}} = 7$ kHz, and a duty cycle of 50%. The average power radiated by the devices through the reflectors system of the measurement setup was acquired with the power meter [65], which presents a sensitivity of -5 dB μW, when performing an OFF–ON–OFF measurement procedure. The characterization of the power meter has been discussed in [53].

The values of measured average power, for different laser power excitations and bias voltages, are shown in Fig. 11 for both prototypes. In order to have a fair comparison between the measured and the estimated values by the model, the readout of the power meter has been divided by the duty cycle factor of the bias voltage signal. The values measured by the detector are compared against the values evaluated by the model as

$$\bar{P}_{\mathrm{meas}}^{\mathrm{theo}} = \frac{1}{2\pi T_p} \int_{-\infty}^{+\infty} E_m(\omega)\, \mathrm{d}\omega \qquad (4)$$

calculated by means of the detected energy spectral density as

$$E_m(\omega) = \eta_{qo}(\omega)\, E_s(\omega) \qquad (5)$$

where η_{qo} is the QO channel efficiency of the measurement setup discussed in Section V-B. Table I highlights the estimated and measured power for $\bar{P}_{\mathrm{laser}} = 500$ mW laser excitation. The values estimated by the model have been obtained by using a transient carriers mobility $\mu = 260$ cm^2/Vs, 210 cm^2/Vs, and 180 cm^2/Vs, for laser power excitations $\bar{P}_{\mathrm{laser}} = 300$ mW,

400 mW, and 500 mW, respectively. These values of transient carriers mobility were found to fit the experimental data in a range of 1 dB for lower bias voltages. The decrease of the transient mobility with excitation power results from a lower effective transient voltage experienced by the photocarriers caused by the large photocurrent. This phenomenon has been reported in the literature as field screening [15], including gap geometries and laser excitation similar to our experiment [66]. The values of transient carriers mobility μ used here are within the range of values expected from the annealed LT-GaAs growing process and inhomogeneity on the same processed wafer (100–300 cm^2/Vs) [67].

From Fig. 11, it can be seen that the measured power increases with laser power and applied bias voltages. Above 60 V per gap, the reduced rate of power increase is thought to be linked to the reduction of the transient carriers mobility due to the Joule heating. In fact, the SI-GaAs substrate, despite absorbing about 3% of the pumping laser power, has a long photocarriers life-time (about 400 ps [68]). Therefore, it provides the biggest contribution to the total average (dc) photocurrent. At higher applied bias voltages, this parasitic photocurrent dissipates more power; the steady-state temperature rises, and the transient carriers mobility accordingly is degraded, as discussed in [68].

An improved modeling of the transient electric field drop, saturation effects, and heating will lead to a better agreement between the theoretical model and the measurements, but this is out of the scope of this paper. These aspects can be object of future modeling and experiments.

Finally, it is worth noting that both devices have been damaged at a laser illumination of 600 mW. Therefore, it was not possible to reach the desired impedance matching between the photoconductive sources and the active impedances of the array cells with the present design.

B. Spectra Measurements

The EO sampling technique [69] has been adopted for measuring the spectra radiated by the PCCA prototypes. A 2-mm-thick ZnTe crystal paired with balanced photodiodes was used. A lock-in amplifier referenced to the emitter bias modulation frequency was used for recording the signal with an integration time of 20 ms. The pulse measurements were performed on a time window of 20 ps, corresponding to a frequency resolution of 50 GHz. The measurements have been carried out in ambient condition without a controlled atmosphere. The amplitude
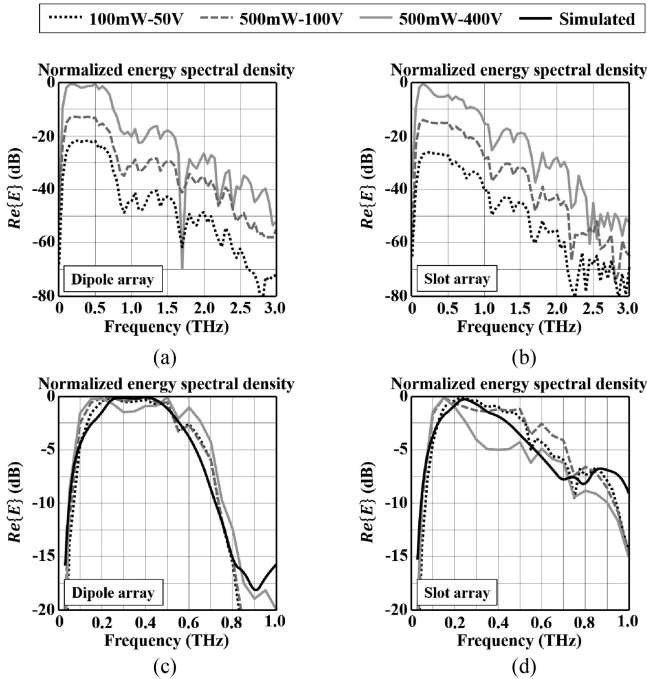
Fig. 12.   Normalized measured energy spectra. (a)–(b) Measured spectra for different bias voltages and laser power excitations on the bandwidth up to 3.0 THz, for dipole and slot array, respectively. The spectra are normalized to the maximum peak value of the spectrum with the highest energy density for both dipole and slot array, respectively. (c)–(d) Comparison between the normalized energy spectral densities for different bias voltages and laser power excitations, and the normalized energy spectral densities radiated by the reflectors system E_r estimated by the model on the array operative bandwidth, for the dipole and slot array, respectively. Each spectrum is normalized to the relevant maximum peak value.

spectra of the measured pulses radiated by the PCCA prototypes under test, for different laser power excitations and bias voltages, are shown in Fig. 12(a) and (b). The spectra are normalized to the maximum peak value of the spectrum with the highest energy density for both dipole and slot array, respectively. Above 3 THz, the measured spectra reach the noise level of the measurement setup, which is below −40 dB with respect to the relevant peak value of the spectrum. This noise is mainly due to the driving laser, which dominates with respect to the noise of the detection electronics. Moreover, in Fig. 12(c) and (d) the normalized spectra are also compared against the normalized real part of the energy spectral density E_r radiated by the reflectors system:

$$E_r(\omega) = \eta_l(\omega)\, \eta_{rs}(\omega)\, E_s(\omega). \qquad (6)$$

The qualitative comparison shows an excellent agreement between the measurements and the estimation of the model for low laser power excitations and bias voltages, in the design bandwidth (≤ 1 THz), thus validating the dispersion analysis performed using our proposed EM model of the QO channel. For frequencies above 0.8 THz, a disagreement between the theoretical model and the measurements is shown. This is due to both the high atmospheric absorption of the THz radiation around 1 THz and the poor radiation efficiency of the array at these frequencies. The spectra for higher laser power excitations and
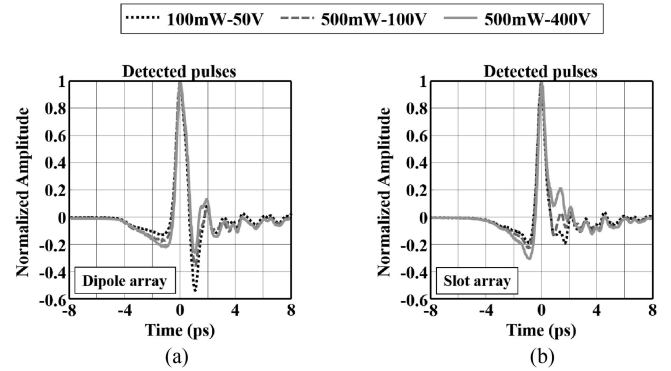

Fig. 13.   Normalized radiated pulses measured by the EO crystal for different laser power excitations and bias voltages. (a) Dipole array. (b) Slot array.

bias voltages present differences with respect to the model, especially for the slot array. The behavior of the radiated spectra as a function of the laser power excitation and bias voltage can be object of future studies.

Fig. 13 shows the relevant normalized pulses radiated by the dipole- and slot-based PCCA prototypes, measured by EO crystal. The amplitude of the pulses have been normalized at the relevant maximum peak value. Both measured spectra and pulses are shown normalized because a calibrated frequency response of the EO crystal is not available, as discussed in [53]. As expected from the different spectra, the figure highlights the different dispersion introduced by the two antenna geometries and the relevant coupling with the QO channel, resulting in different shapes of the pulses. Moreover, the figure also shows how the change of the optical excitation and applied bias voltage affects the shape of the pulses. These changes are not related to the antenna dispersion, but to different carrier transport phenomena occurring in the photoconductive material.

C. Performance Comparison Against a Single Bow-Tie PCA

A single bow-tie antenna was used as a reference for comparing the performances of the arrays with respect to a single antenna, with the same geometrical features discussed in [51] and [53], manufactured on the same LT-GaAs wafer of the arrays. In details, it presents a gap of $10 \times 10\,\mu$m side length, and a tapering angle of $90°$. A focusing lens for collimating the laser beam on the gap of the antenna was used, obtaining a focused laser beam diameter of about $D_{\text{laser}} = 14.5\,\mu$m, measured by the knife-edge technique.

The maximum measured average power was 241 μW by using 100 mW of laser power excitation and 100 V of bias voltage. Table I lists the estimated and measured power for 100 mW laser excitation. The values estimated by the model have been obtained by using a transient carriers mobility $\mu = 100\,\text{cm}^2/\text{Vs}$, which is within the range of transient carriers mobility values expected from the annealed LT-GaAs growing process [67]. This value of transient mobility is lower than the ones used for the arrays, since the laser power density on the gap of the bow-tie antenna is higher than the laser power density on the array gaps, according to the discussion in Section VI-A. Indeed, for the

maximum laser and voltage excitations, the array unit cells are excited by an optical power lower than $\bar{P}_{\text{laser}}^{\text{cell}} = 9.6$ mW (laser power exciting the central unit cell of the array), and a bias voltage $V_{\text{bias}}^{\text{cell}} = 80$ V; whereas, the bow-tie gap is excited by a laser power $\bar{P}_{\text{laser}} = 100$ mW, and a bias voltage $V_{\text{bias}} = 100$ V.

Fig. 11(c) shows the measured power radiated by the bow-tie antenna for different laser power excitations and different voltages. Saturation effects due to the high laser excitation and bias voltages are evident from the measurements, limiting the possibility of obtaining a substantial increase of average power from single antenna devices, before the thermal and voltage breakdown failure. The maximum measured power of the bow-tie is 3 and 2 times less than the maximum measured power of the dipole and slot array, respectively (see Table I). It is worth noting that, as shown in [51] and [53], the energy of the bow-tie antenna, measured by the detector, is spread on a spectral bandwidth larger than the one at which the arrays are designed, 0.1 THz–2 THz [51], [53], whereas the measured energy spectra of the arrays are spread on the bandwidth less than 1 THz. The array can be designed over a larger bandwidth, up to 2 THz, by reducing the period of the cells and integrating the microlenses array directly on the antenna structure, resulting in an increase of the radiated power.

VII. CONCLUSION

In this paper, an architecture for pulsed PCAs, which provides clean radiation patterns and high radiation efficiency over a large bandwidth, is presented. The solution realized a connected array of sources, by implementing an "ad hoc" bias voltage structure, and an optical system to excite the devices. Two prototypes have been designed to maximize the power radiated on a selected bandwidth smaller than the one where the photoconductor source generates energy, effectively realizing a low band-pass filter. Two PCCA demonstrators, working on an operative bandwidth at -5 dB from 0.1 to 0.6 THz, have been designed and fabricated. The prototypes have been characterized by power and spectrum measurements, which are in good agreement with the simulated results, thus, validating the effectiveness of the proposed solution for the enhancement of the radiated power for PCAs. The maximum THz average power generated reaches the order of mW. The demonstrated power levels are obtained only optimizing the antenna architectures and the relevant modeling. Since the photoconductive source generates pulses, whose energy is spread over a bandwidth up to 2 THz, [51], [53], an improvement of the performances, in terms of radiated power and larger bandwidth, can be obtained by designing array devices with smaller periodicity, thus, enlarging the operative bandwidth of the array. Therefore, a microlens array with a smaller pitch is needed. This solution can be obtained by integrating microlenses directly on the antenna array structure, allowing also a reduction of the complexity of the current assembly for focusing the laser beam on the photoconductive gaps. Moreover, in order to overcome the alignment problem and for reducing the spillover between the laser beam and the device, a solution based on optic fiber coupling could be adopted [70], paying attention to the dispersion of the optic fiber,
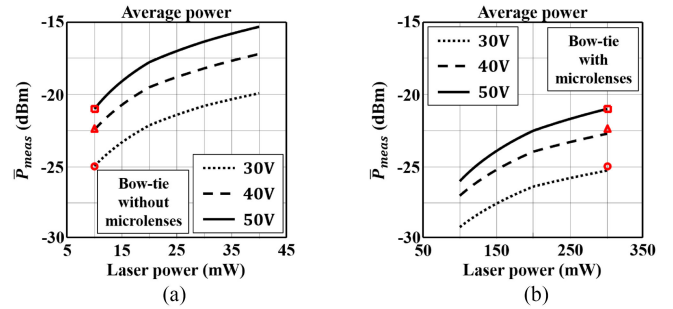

Fig. 14. Measured average power versus laser power excitations for different applied bias voltage of the bow-tie antennas for the retrieval of the laser spot focused by the microlenses array. (a) Bow-tie without microlenses array. (b) Bow-tie with microlenses array. The three red markers in the figures identify the working points where the two devices radiate the same amount of average power.

when working in a pulsed mode. Finally, should one be able to adopt more efficient photoconductive excitation of carriers [40], the resulting power level generated could be even higher.

APPENDIX A
FOCUSING PERFORMANCE OF THE MICROLENSES ARRAY VIA POWER MEASUREMENTS OF A PHOTOCONDUCTIVE BOW-TIE ANTENNA

Because it was not possible to measure the focusing performance of the microlenses array directly, by using the knife-edge technique, once that the PCCA array were assembled, a different approach has been used. Two bow-tie antenna prototypes with the same geometrical features discussed in [51] and [53] were also manufactured on the same LT-GaAs wafer. The bow-tie antennas present a gap of $10\,\mu\text{m} \times 10\,\mu\text{m}$ side length and a tapering angle of $90°$. An array of microlenses was mounted on one of the bow-tie antennas, and a comparison of the radiated average power with the bow-tie antenna without microlenses array was conducted in order to estimate the size of the laser spot focused by the microlenses. The procedure and the measurement setup used for this experiment were the same discussed in Section IV.

In the case of the bow-tie without a microlenses array, the focused laser beam diameter was the same discussed in Section VI-C ($D_{\text{laser}} = 14.5\,\mu\text{m}$). In Fig. 14(a), the measured average power of the bow-tie antenna with respect to the laser power excitation is shown for three different applied bias voltages. Moreover, in the figure three markers identify the amount of measured average power, when the laser beam excitation was 10 mW. By considering the spillover efficiency of the laser beam with respect to the gap area, the amount of laser power excitation on the gap was about 3.4 mW. We used this value as reference for estimating the dimension of the spot focused by the microlenses array.

The bow-tie with microlenses array was illuminated by the same laser beam used for the array measurements with diameter $D_{\text{laser}} = 660\,\mu\text{m}$, discussed in Section IV. Fig. 14(b) shows the average power measured by this device versus the laser power excitation for the same three different bias voltages used for the bow-tie device without the microlenses array. It is worth
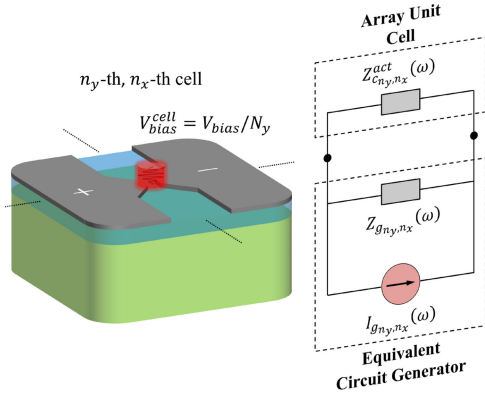
Fig. 15.   Array unit cell and relevant Norton equivalent circuit representation.

noting that the laser power used for the excitation of this device is spread on an area much larger than the one used for the device without microlenses. Therefore, in order to obtain the same amount of average radiated power, higher values of laser power have to be used. The bow-tie illuminated by the microlenses array radiated the same power of the device without the microlenses array in correspondence of an average laser excitation of 300 mW. The amount of laser power captured by the unit cell of the microlenses array, aligned to the antenna gap and centered with respect to the laser beam axis, is about 6 mW. Taking into account of the transmission losses of the microlenses array (4%) and of the spillover efficiency on the gap, in order to have the same average power impinging on the photoconductive gap of the bow-tie without the microlenses array (3.4 mW), the laser spot diameter at -3 dB focused by the microlenses array has to be about 10 μm, which is larger with respect to the ideal value of the focused spot (7.5 μm), as discussed in Section III. In Fig. 14(b), the markers highlight the points where the bow-tie antenna with the microlenses array radiates the same amount of average power of the bow-tie without the microlenses array.

APPENDIX B
ENERGY RADIATED BY A PHOTOCONDUCTIVE ARRAY ANTENNA

The simulated active impedances $Z_{c_{n_y,n_x}}^{\mathrm{act}}$ of each array cell n_y, n_x have been used for computing the active energy spectra associated to each array cell as in [51]

$$
\begin{aligned}
&E_{s_{n_y,n_x}}^{\mathrm{act}}(\omega)\\
&= Z_{c_{n_y,n_x}}^{\mathrm{act}}(\omega)\left|\frac{Z_{g_{n_y,n_x}}(\omega)}{Z_{c_{n_y,n_x}}^{\mathrm{act}}(\omega) + Z_{g_{n_y,n_x}}(\omega)}\right|^2 \left|I_{g_{n_y,n_x}}(\omega)\right|^2
\end{aligned}
$$
(B.1)

where $Z_{g_{n_y,n_x}}$ and $I_{g_{n_y,n_x}}$ are the equivalent impedance and current spectrum generator of the n_y th, n_xth photoconductive source of the array cell, evaluated according to each laser beam excitation (see Fig. 15). Assuming that the antenna array is lossless, the real part of $E_{s_{n_y,n_x}}^{\mathrm{act}}$ is associated to the energy radiated by the n_y th, n_xth cell of the array [51]. The total energy spectrum generated by the array can be estimated by summing the

energy spectra radiated by all the array cells as discussed in [71] and [72]

$$
E_s(\omega) = \sum_{n_y=-\frac{N_y-1}{2}}^{\frac{N_y-1}{2}} \sum_{n_x=-\frac{N_x-1}{2}}^{\frac{N_x-1}{2}} E_{s_{n_y,n_x}}^{\mathrm{act}}(\omega)
$$
(B.2)

where N_y and N_x are the number of the array elements along y and x direction, respectively.

Defining the matching efficiency $\eta_{m_{n_y,n_x}}$ of the n_y th, n_xth array cell as the ratio between the energy spectral density $E_{s_{n_y,n_x}}^{\mathrm{act}}$ radiated by the n_y th, n_xth array cell and the energy spectral density $E_{s_{n_y,n_x}}^{\max}$ of the maximum available energy provided by the relevant photoconductor gap to a matched load array cell, the active energy spectral density $E_{s_{n_y,n_x}}^{\mathrm{act}}$ can be expressed also as

$$
E_{s_{n_y,n_x}}^{\mathrm{act}}(\omega) = \eta_{m_{n_y,n_x}}(\omega) E_{s_{n_y,n_x}}^{\max}(\omega)
$$
(B.3)

and the energy spectral density $E_s^{\max}$ of the maximum available energy provided by the photoconductor gaps to a matched loads array can be defined as

$$
E_s^{\max}(\omega) = \sum_{n_y=-\frac{N_y-1}{2}}^{\frac{N_y-1}{2}} \sum_{n_x=-\frac{N_x-1}{2}}^{\frac{N_x-1}{2}} E_{s_{n_y,n_x}}^{\max}(\omega)
$$
(B.4)

ACKNOWLEDGMENT

REFERENCES

[1] P. Jepsen, D. Cooke, and M. Koch, "Terahertz spectroscopy and imaging modern techniques and applications," *Laser Photon. Rev.*, vol. 5, no. 1, pp. 124–166, Jan. 2011, doi: 10.1002/lpor.201000011.

[2] D. Saeedkia Ed., *Handbook of Terahertz Technology for Imaging, Sensing and Communications* (Series Woodhead Publishing Series in Electronic and Optical Materials). Amsterdam, The Netherlands: Elsevier, 2013.

[3] S. Preu *et al.*, "Principles of THz generation," in *Semiconductor Terahertz Technology: Devices and Systems at Room Temperature Operation*, G. Carpintero, E. G.-M. noz, H. L. Hartnagel, and A. V. R. S. Preu, Eds. Hoboken, NJ, USA: Wiley, 2015, pp. 3–68.

[4] M. Hangyo, M. Tani, T. Nagashima, H. Kitahara, and H. Sumikura, "Spectroscopy and imaging by laser excited terahertz waves," *Plasma Fusion Res.*, vol. 2, Nov. 2007, Art. no. S1020, doi: 10.1585/pfr.2.S1020.

[5] J. F. Federici *et al.*, "THz imaging and sensing for security applications, explosives, weapons and drugs," *Semicond. Sci. Technol.*, vol. 20, no. 7, pp. S266–S280, Jul. 2005, doi: 10.1088/0268-1242/20/7/018.

[6] M. K. Choi, A. Bettermann, and D. W. van der Weide, "Potential for detection of explosive and biological hazards with electronic terahertz systems," *Philos. Trans. Roy. Soc. London A, Math., Physical Eng. Sci.*, vol. 362, no. 1815, pp. 337–349, Feb. 2004, doi: 10.1098/rsta.2003.1319.

[7] M. C. Kemp *et al.*, "Security applications of terahertz technology," in *Terahertz for Military and Security Applications* (Series Proceedings SPIE), vol. 5070, Apr. 2003, pp. 44–52, doi: 10.1117/12.500491.

[8] P. H. Siegel, "Terahertz technology in biology and medicine," *IEEE Trans. Microw. Theory Techn.*, vol. 52, no. 10, pp. 2438–2447, Oct. 2004, doi: 10.1109/MWSYM.2004.1338880.

[9] P. F. Taday, "Applications of terahertz spectroscopy to pharmaceutical sciences," *Philos. Trans. Roy. Soc. London A, Math., Physical Eng. Sci.*, vol. 362, no. 1815, pp. 351–364, Feb. 2004, doi: 10.1098/rsta.2003.1321.

[10] T. Globus *et al.*, "THz-frequency spectroscopic sensing of DNA and related biological materials," *Int. J. High Speed Electron. Syst.*, vol. 13, no. 4, pp. 903–936, Dec. 2003, doi: 10.1142/S0129156403002083.

[11] D. Mittleman Ed., *Sensing With Terahertz Radiation* (Series Springer Series in Optical Sciences), vol. 85. Berlin, Germany: Springer-Verlag, 2003.

[12] J. W. Bowen, "Towards terahertz communications—Systems requirements," in *Terahertz Sources and Systems*, R. E. Miles, P. Harrison, and D. Lippens, Eds. Dordrecht, The Netherland: Springer, 2001, pp. 269–283, doi: 10.1007/978-94-010-0824-217.

[13] D. Grischkowsky, S. Keiding, M. van Exter, and C. Fattinger, "Far-infrared time-domain spectroscopy with terahertz beams of dielectrics and semiconductors," *J. Opt. Soc. Am. B*, vol. 7, no. 10, pp. 2006–2015, Oct. 1990, doi: 10.1364/JOSAB.7.002006.

[14] D. H. Auston, K. P. Cheung, and P. R. Smith, "Picosecond photoconducting Hertzian dipoles," *Appl. Phys. Lett.*, vol. 45, no. 3, pp. 284–286, Aug. 1984, doi: 10.1063/1.95174.

[15] P. U. Jepsen, R. H. Jacobsen, and S. R. Keiding, "Generation and detection of terahertz pulses from biased semiconductor antennas," *J. Opt. Soc. Am. B*, vol. 13, no. 11, pp. 2424–2436, Nov. 1996, doi: 10.1364/JOSAB.13.002424.

[16] M. Tani, S. Matsuura, K. Sakai, and S. Nakashima, "Emission characteristics of photoconductive antennas based on low-temperature-grown GaAs and semi-insulating GaAs," *Appl. Opt.*, vol. 36, no. 30, pp. 7853–7859, Oct. 1997, doi: 10.1364/AO.36.007853.

[17] H. Roehle *et al.*, "Next generation 1.5 μm terahertz antennas: Mesa-structuring of InGaAs/InAlAs photoconductive layers," *Opt. Express*, vol. 18, no. 3, pp. 2296–2301, Feb. 2010, doi: 10.1364/OE.18.002296.

[18] A. Cho and J. Arthur, "Molecular beam epitaxy," *Prog. Solid State Chemistry*, vol. 10, pp. 157–191, 1975, doi: 10.1016/0079-6786(75)90005-9.

[19] P. R. Smith, D. H. Auston, A. M. Johnson, and W. M. Augustyniak, "Picosecond photoconductivity in radiation-damaged silicon-on-sapphire films," *Appl. Phys. Lett.*, vol. 38, no. 1, pp. 47–50, Jan. 1981, doi: 10.1063/1.92128.

[20] M. C. Nuss, D. H. Auston, and F. Capasso, "Direct subpicosecond measurement of carrier mobility of photoexcited electrons in gallium arsenide," *Physical Rev. Lett.*, vol. 58, pp. 2355–2358, Jun. 1987, doi: 10.1103/PhysRevLett.58.2355.

[21] P. R. Smith, D. H. Auston, and M. C. Nuss, "Subpicosecond photoconducting dipole antennas," *IEEE J. Quantum Electron.*, vol. 24, no. 2, pp. 255–260, Feb. 1988, doi: 10.1109/3.121.

[22] B. B. Hu, X. Zhang, and D. H. Auston, "Temperature dependence of femtosecond electromagnetic radiation from semiconductor surfaces," *Appl. Phys. Lett.*, vol. 57, no. 25, pp. 2629–2631, Dec. 1990, doi: 10.1063/1.103829.

[23] X. Zhang and D. H. Auston, "Optoelectronic measurement of semiconductor surfaces and interfaces with femtosecond optics," *J. Appl. Phys.*, vol. 71, no. 1, pp. 326–338, Jan. 1992, doi: 10.1063/1.350710.

[24] I. S. Gregory *et al.*, "High resistivity annealed low-temperature GaAs with 100 fs lifetimes," *Appl. Phys. Lett.*, vol. 83, no. 20, pp. 4199–4201, Nov. 2003, doi: 10.1063/1.1628389.

[25] N. Llombart and A. Neto, "THz time-domain sensing: The antenna dispersion problem and a possible solution," *IEEE Trans. THz Sci. Technol.*, vol. 2, no. 4, pp. 416–423, Jul. 2012, doi: 10.1109/TTHZ.2012.2197949.

[26] G. Chattopadhyay, "Technology, capabilities, and performance of low power terahertz sources," *IEEE Trans. THz Sci. Technol.*, vol. 1, no. 1, pp. 33–53, Sep. 2011, doi: 10.1109/TTHZ.2011.2159561.

[27] J. V. Siles *et al.*, "A new generation of room-temperature frequency multiplied sources with up to 10× higher output power in the 160-GHz – 1.6-THz range," *IEEE Trans. THz Sci. Technol.*, vol. 8, no. 6, pp. 596–604, Nov. 2018, doi: 10.1109/TTHZ.2018.2876620.

[28] J. T. Darrow, X. C. Zhang, and D. H. Auston, "Power scaling of large-aperture photoconducting antennas," *Appl. Phys. Lett.*, vol. 58, no. 1, pp. 25–27, Jan. 1991, doi: 10.1063/1.104426.

[29] J. T. Darrow, X. C. Zhang, D. H. Auston, and J. D. Morse, "Saturation properties of large-aperture photoconducting antennas," *IEEE J. Quantum Electron.*, vol. 28, no. 6, pp. 1607–1616, Jun. 1992, doi: 10.1109/3.135314.

[30] P. K. Benicewicz, J. P. Roberts, and A. J. Taylor, "Scaling of terahertz radiation from large-aperture biased photoconductors," *J. Opt. Soc. Am. B*, vol. 11, no. 12, pp. 2533–2546, Dec. 1994, doi: 10.1364/OL.18.001332.

[31] H. Yoneda, K. Tokuyama, K. Ueda, H. Yamamoto, and K. Baba, "High-power terahertz radiation emitter with a diamond photoconductive switch array," *Appl. Opt.*, vol. 40, no. 36, pp. 6733–6736, Dec. 2001, doi: 10.1364/AO.40.006733.

[32] A. Dreyhaupt, S. Winnerl, T. Dekorsy, and M. Helm, "High-intensity terahertz radiation from a microstructured large-area photoconductor," *Appl. Phys. Lett.*, vol. 86, no. 12, Mar. 2005, Art. no. 121114, doi: 10.1063/1.1891304.

[33] M. Beck *et al.*, "Impulsive terahertz radiation with high electric fields from an amplifier-driven large-area photoconductive antenna," *Opt. Express*, vol. 18, no. 9, pp. 9251–9257, Apr. 2010, doi: 10.1364/OE.18.009251.

[34] M. Awad, M. Nagel, H. Kurz, J. Herfort, and K. Ploog, "Characterization of low temperature GaAs antenna array terahertz emitters," *Appl. Phys. Lett.*, vol. 91, no. 18, Oct. 2007, Art. no. 181124, doi: 10.1063/1.2800885.

[35] G. Matthäus *et al.*, "Microlens coupled interdigital photoconductive switch," *Appl. Phys. Lett.*, vol. 93, no. 9, Sep. 2008, Art. no. 091110, doi: 10.1063/1.2976162.

[36] B. Pradarutti *et al.*, "Terahertz line detection by a microlens array coupled photoconductive antenna array," *Opt. Express*, vol. 16, no. 22, pp. 18 443–18 450, Oct. 2008, doi: 10.1364/OE.16.018443.

[37] H. F. Tiedje, D. Saeedkia, M. Nagel, and H. K. Haugen, "Optical scanning techniques for characterization of terahertz photoconductive antenna arrays," *IEEE Trans. Microw. Theory Techn.*, vol. 58, no. 7, pp. 2040–2045, Jul. 2010, doi: 10.1109/TMTT.2010.2050388.

[38] S. Preu *et al.*, "1550 nm ErAs:In(Al)GaAs large area photoconductive emitters," *Appl. Phys. Lett.*, vol. 101, no. 10, Sep. 2012, Art. no. 101105, doi: 10.1063/1.4750244.

[39] P. J. Hale *et al.*, "20 THz broadband generation using semi-insulating GaAs interdigitated photoconductive antennas," *Opt. Express*, vol. 22, no. 21, pp. 26 358–26 364, Oct. 2014, doi: 10.1364/OE.22.026358.

[40] N. T. Yardimci, S. H. Yang, C. W. Berry, and M. Jarrahi, "High-power terahertz generation using large-area plasmonic photoconductive emitters," *IEEE Trans. THz Sci. Technol.*, vol. 5, no. 2, pp. 223–229, Mar. 2015, doi: 10.1109/TTHZ.2015.2395417.

[41] A. Garufo, G. Carluccio, N. Llombart, and A. Neto, "Design of photoconductive connected arrays for pulsed terahertz radiation," in *Proc. 10th Eur. Conf. Antennas Propag.*, Apr. 2016, Davos, Switzerland.

[42] A. Neto, A. Garufo, G. Carluccio, and N. Llombart, "Photoconductive antenna array," Feb. 2017, WO Patent App. PCT/NL2016/050,567. [Online]. Available: https://encrypted.google.com/patents/WO2017 023172A1?cl=ko

[43] A. Neto and J. J. Lee, "Infinite bandwidth" long slot array antenna," *IEEE Antennas Wireless Propag. Lett.*, vol. 4, pp. 75–78, Jun. 2005, doi: 10.1109/LAWP.2005.844141.

[44] A. Neto and J. J. Lee, "Ultrawide-band properties of long slot arrays," *IEEE Trans. Antennas Propag.*, vol. 54, no. 2, pp. 534–543, Feb. 2006, doi: 10.1109/TAP.2005.863140.

[45] A. Neto, D. Cavallo, G. Gerini, and G. Toso, "Scanning performances of wideband connected arrays in the presence of a backing reflector," *IEEE Trans. Antennas Propag.*, vol. 57, no. 10, pp. 3092–3102, Oct. 2009, doi: 10.1109/TAP.2009.2028631.

[46] D. Cavallo, A. Neto, and G. Gerini, "Green's function based equivalent circuits for connected arrays in transmission and in reception," *IEEE Trans. Antennas Propag.*, vol. 59, no. 5, pp. 1535–1545, May 2011, doi: 10.1109/TAP.2011.2123063.

[47] D. Cavallo and A. Neto, "A connected array of slots supporting broadband leaky waves," *IEEE Trans. Antennas Propag.*, vol. 61, no. 4, pp. 1986–1994, Apr. 2013, doi: 10.1109/TAP.2012.2236635.

[48] O. Yurduseven, D. Cavallo, and A. Neto, "Wideband dielectric lens antenna with stable radiation patterns fed by coherent array of connected leaky slots," *IEEE Trans. Antennas Propag.*, vol. 62, no. 4, pp. 1895–1902, Apr. 2014, doi: 10.1109/TAP.2014.2298875.

[49] O. Yurduseven, D. Cavallo, A. Neto, G. Carluccio, and M. Albani, "Parametric analysis of extended hemispherical dielectric lenses fed by a broadband connected array of leaky-wave slots," *IET Microw., Antennas Propag.*, vol. 9, no. 7, pp. 611–617, May 2015, doi: 10.1049/iet-map.2014.0403.

[50] N. M. Froberg, B. B. Hu, X.-C. Zhang, and D. H. Auston, "Terahertz radiation from a photoconducting antenna array," *IEEE J. Quantum Electron.*, vol. 28, no. 10, pp. 2291–2301, Oct. 1992, doi: 10.1109/3.159536.

[51] A. Garufo, G. Carluccio, N. Llombart, and A. Neto, "Norton equivalent circuit for pulsed photoconductive antennas—Part I: Theoretical model," *IEEE Trans. Antennas Propag.*, vol. 66, no. 4, pp. 1635–1645, Apr. 2018, doi: 10.1109/TAP.2018.2800524.

[52] C. W. Berry, M. R. Hashemi, and M. Jarrahi, "Generation of high power pulsed terahertz radiation using a plasmonic photoconductive emitter array with logarithmic spiral antennas," *Appl. Phys. Lett.*, vol. 104, no. 8, Feb. 2014, Art. no. 081122, doi: 10.1063/1.4866807.

[53] A. Garufo *et al.*, "Norton equivalent circuit for pulsed photoconductive antennas—Part II: Experimental validation," *IEEE Trans. Antennas Propag.*, vol. 66, no. 4, pp. 1646–1659, Apr. 2018, doi: 10.1109/TAP.2018.2800704.

[54] "RPC Photonics Inc." Rochester, NY, USA, 2018.

[55] G. Chattopadhyay, A. Freni, N. Llombart, and A. Neto, "Reflector antennas for terahertz imaging applications," in *Handbook of Reflector Antennas and Feed Systems Volume III: Applications of Reflectors*, S. Rao, L. Shafai, and S. K. Sharma, Eds. Norwood, MA, USA: Artech House, 2013, pp. 145–211.

[56] "Sumipro Submicron Lathing BV." Almelo, The Netherlands.

[57] "SCS Germany GmbH." Pliezenhausen, Germany.

[58] [Online]. Available: http://www.latticematerials.com/blog/portfolio/electrical-properties-of-silicon," Lattice Materials, Bozeman, MT, USA.

[59] "Veldlaser," S-Heerenberg, The Netherlands.

[60] "Standa Ltd." Vilnius, Lithuania.

[61] "CST Microwave Studio 2012," [Online]. Available: http://www.cst.com.

[62] D. F. Filipovic, S. S. Gearhart, and G. M. Rebeiz, "Double-slot antennas on extended hemispherical and elliptical silicon dielectric lenses," *IEEE Trans. Microw. Theory Techn.*, vol. 41, no. 10, pp. 1738–1749, Oct. 1993, doi: 10.1109/22.247919.

[63] "GRASP 10.5.0," [Online]. Available: http://www.ticra.com.

[64] P. H. Bolivar *et al.*, "Measurement of the dielectric constant and loss tangent of high dielectric-constant materials at terahertz frequencies," *IEEE Trans. Microw. Theory Techn.*, vol. 51, no. 4, pp. 1062–1066, Apr. 2003, doi: 10.1109/TMTT.2003.809693.

[65] "Virginia Diodes Inc." Charlottesville, VA, USA, 2018.

[66] M. Tonouchi, "Cutting-edge terahertz technology," *Nature Photon.*, vol. 1, no. 2, pp. 97–105, Feb. 2007, doi: 10.1038/nphoton.2007.3.

[67] M. Tani, M. Herrmann, and K. Sakai, "Generation and detection of terahertz pulsed radiation with photoconductive antennas and its application to imaging," *Meas. Sci. Technol.*, vol. 13, no. 11, p. 1739–1745, 2002, doi: 10.1088/0957-0233/13/11/310.

[68] D. R. Bacon *et al.*, "Free-space terahertz radiation from a lt-gaas-on-quartz large-area photoconductive emitter," *Opt. Express*, vol. 24, no. 23, pp. 26 986–26 997, Nov. 2016, doi: 10.1364/OE.24.026986.

[69] J. Valdmanis and G. Mourou, "Subpicosecond electrooptic sampling: Principles and applications," *IEEE J. Quantum Electron.*, vol. QE-22, no. 1, pp. 69–78, Jan. 1986, doi: 10.1109/JQE.1986.1072867.

[70] S. Preu *et al.*, "Fiber-coupled 2-D n-i-pn-i-p superlattice photomixer array," *IEEE Trans. Antennas Propag.*, vol. 65, no. 7, pp. 3474–3480, Jul. 2017, doi: 10.1109/TAP.2017.2700039.

[71] D. Pozar, Y.-W. Kang, D. Schaubert, and R. McIntosh, "Optimization of the transient radiation from a dipole array," *IEEE Trans. Antennas Propag.*, vol. AP-33, no. 1, pp. 69–75, Jan. 1985, doi: 10.1109/TAP.1985.1143478.

[72] Y.-W. Kang and D. Pozar, "Optimization of pulse radiation from dipole arrays for maximum energy in a specified time interval," *IEEE Trans. Antennas Propag.*, vol. AP-34, no. 12, pp. 1383–1390, Dec. 1986, doi: 10.1109/TAP.1986.1143772.

Paolo Maria Sberna was born in Palermo, Italy, in 1987. He received the bachelor's degree in physics (cum laude) from the University of Catania, Catania, Italy, in 2009, with a thesis on Bose–Einstein condensation, the master's degree in physics (cum laude) from the University of Catania, in 2011, with the thesis Quantum confinement effects on Si nano-crystals observed with Raman spectroscopy, and the Ph.D. degree from the University of Catania and partly from the NOVA University of Lisbon, Lisbon, Portugal, in 2015, with the thesis Novel Approaches to Photoactive Nano-structured Materials for Efficient Solar Cells.

Since May 2015, he has been with the Delft University of Technology (TU Delft), Delft, The Netherlands. The topic covered during the first two years has been low-temperature Si thin-film transistors fabrication by solution-processing. Since 2017, he has been working on III-V photoconductive antennas for THz applications with the Terahertz Sensing Group, Microelectronic Department, TU Delft. Since September 2018, he has been Equipment Responsible Scientist with the Else Kooi Laboratory, TU Delft. His research interests are solid-state physics, material science, chemistry, and microfabrication.

Giorgio Carluccio (M'19) was born in 1979 and grew up in Ortelle, Italy. He received the Laurea degree in telecommunications engineering and the Ph.D. degree in information engineering from the University of Siena, Siena, Italy, in 2006 and 2010, respectively.

In 2008 and 2009, he was an Invited Visiting Scholar with the ElectroScience Laboratory, Department of Electrical and Computer Engineering, The Ohio State University, Columbus, OH, USA. From 2010 to 2012 and from 2013 to 2014, he was a Researcher with the Department of Information Engineering and Mathematics, University of Siena. From 2012 to 2013, he was a Researcher with the Department of Electronics and Telecommunication, University of Florence, Florence, Italy. In 2012 and 2013, he was a Visiting Researcher with the Department of Microelectronics, Delft University of Technology (TU Delft), Delft, The Netherlands, where he also was a Researcher from 2014 to 2018. Since 2018, he has been a RF circuits and antenna Scientist with NXP Semiconductors, Eindhoven, The Netherlands, where he focuses on antenna-in-package and RF devices for automotive radar applications. His research interests deal with electromagnetic wave theory, mainly focused on asymptotic high-frequency techniques for electromagnetic scattering and propagation; and with modeling and design of antennas: mainly, dielectric lens antennas, reflectarray antennas, and THz antennas based on photoconductive materials.

Dr. Carluccio was the recipient of the 2018 EurAAP International "Leopold B. Felsen Award for Excellence in Electrodynamics," and of the 2010 URSI Commission B Young Scientist Award at the International Symposium on Electromagnetic Theory (EMTS 2010), where he also received the third prize for the Young Scientist Best Paper Award.

Alessandro Garufo (S'13–M'17) received the B.Sc. and M.Sc. degrees in telecommunication engineering from the University of Siena, Siena, Italy, in 2007 and 2012, respectively, and the Ph.D. degree in applied electromagnetism and THz technology from the Delft University of Technology, Delft, The Netherlands, in 2017.

From 2011 until 2012, he was an intern with the Antenna Group, Thales Alenia Space, Rome, Italy, where he developed his M.Sc. degree thesis. In 2012, he was a Researcher with the Applied Electromagnetic Laboratory (LEA), University of Siena, Siena, Italy. From 2012 to 2018, he was with the THz Sensing Group, Microelectronics Department, Delft University of Technology, Delft, The Netherlands, as a Ph.D. Researcher and thereafter as a Postdoctoral Researcher. From 2013 until 2014, he was a Visiting Scholar with the Metamaterials and Plasmonics Research Laboratory, University of Texas at Austin, Austin, TX, USA. In 2018, he joined, as a Research Scientist, the Radar Technology Group, TNO Defense, Security and Safety, The Hague, The Netherlands. His research interest includes analysis and design of antennas, dielectric lens antennas, and antenna arrays with emphasis at THz frequencies based on photoconductive sources.

Joshua R. Freeman received the M.Phys. (Hons.) degree in physics from the University Of Oxford, Oxford, U.K., in 2005, and the Ph.D. degree from the University of Cambridge, Cambridge, U.K., in 2010.

In 2010, he started a Postdoctoral Fellowship with the Cavendish, supported by the EPSRC. In 2011, won an individual intra-European fellowship and took up the Marie Curie position at the Ecole Normale Supérieure in Paris, returning to the U.K. to take up a postdoctoral research fellowship at the University of Leeds. In April 2016, he was awarded a "University Academic Fellowship" at the University of Leeds. His research interests include the active region design, modelocking, injection locking and coherent detection of quantum cascade lasers, and terahertz devices for time-domain spectroscopy and high-resolution continuous-wave spectroscopy.

David R. Bacon received the M.Eng. and Ph.D. degrees in electronic and electrical engineering, in 2013 and 2017, respectively, both from the University of Leeds, Leeds, U.K.

In 2017, after receiving a letter of recognition of research excellence for his Ph.D. thesis, he was appointed as an EPSRC Doctoral Prize Fellow at the Pollard Institute, School of Electronic and Electrical Engineering, University of Leeds, Leeds, U.K. His research interests include the generation and use of high-field terahertz radiation, time-domain spectroscopy and terahertz quantum cascade lasers.

Jochem J. A. Baselmans received the graduate and Ph.D. degrees (summa cum laude) from the University of Groningen, Groningen, The Netherlands, in 1998 and 2002, respectively. His doctoral dissertation was entitled Controllable Josephson Junctions.

He started working as a Postdoctoral Instrument Scientist with SRON Netherlands Institute for Space Research, in 2002, where he was until 2004 involved with hot electron bolometer mixers. In 2005, he joined SRON, Utrecht, The Netherlands, and started working on microwave kinetic inductance detectors after a three-month visit to the California Institute of Technology, Pasadena, CA, USA. He is a Senior Instrument Scientist with the SRON Netherlands Institute for Space Research, Utrecht, The Netherlands, where since 2002, he has been with the Technology Division. Since 2015, he has also been an Associate Professor with the THz Sensing Group, Delft University of Technology, Delft, The Netherlands. He has authored in excess of 100 papers. He now leads the Dutch effort on the development of microwave kinetic inductance detectors, where his main research interests include ultrasensitive MKIDs for THz radiation detection and advanced on-chip imaging spectrometers for sub-THz imaging spectroscopy.

Dr. Baselmans was the recipient of an ERC Consolidator Grant in 2015 to develop an advanced imaging spectrometer based upon MKIDs.

Lianhe Li photograph and biography not available at the time of publication.

Edmund H. Linfield received the B.A. (Hons.) degree in physics and the Ph.D. degree from the University of Cambridge, Cambridge, U.K., in 1986 and 1991, respectively.

He continued his research with the Cavendish Laboratory, University of Cambridge, becoming an Assistant Director of Research and a Fellow of Gonville and Caius College, Cambridge, U.K., in 1997. In 2004, he joined the University of Leeds, Leeds, U.K., to take up the Chair of Terahertz Electronics, where he is currently also the Director of Research and Innovation with the School of Electronic and Electrical Engineering. His research interests include semiconductor growth and device fabrication, terahertz-frequency optics and electronics, and nanotechnology.

Prof. Linfield shared the Faraday Medal and Prize from the Institute of Physics in 2014, and was the recipient of the Wolfson Research Merit Award from the Royal Society in 2015.

Juan Bueno received the graduate degree in physics from the University of Cantabria, Santander, Spain, in 2003, and the Ph.D. degree from the University of Leiden, Leiden, The Netherlands, in 2007. During his Ph.D. degree studies, he studied quantum crystals at very low temperatures.

From 2007 to 2008, he was a Postdoctoral Fellow with the University of California, San Diego, CA, USA, continuing his work on quantum crystals. In 2008, he made the decision to switch research topics and interests from fundamental physics to the study of superconducting devices. He was awarded with a NASA Postdoctoral position (NPP), becoming a Postdoc with the Jet Propulsion Laboratory (USA) until 2010. During this time, he pioneered a new type of pair-breaking radiation detector, the Quantum Capacitance Detector. After his time with JPL, he joined the Center for Astrobiology (Spain) in 2010 after receiving a JAE-doc grant, working mainly on kinetic inductance detectors (KIDs). He became an Instrument Scientist with SRON - Netherlands Institute for Space Research (The Netherlands), in 2012, working on the development of KIDs for sub-mm wave and far IR space-based observatories. He has published more than 30 peer-reviewed papers, a third of them as the first author. His research interest concentrates on the development of ultrasensitive broadband KIDs for future space-based missions.

Alexander G. Davies received the B.Sc. (Hons.) degree in chemical physics from the University of Bristol, Bristol, U.K., in 1987, and the Ph.D. degree from the University of Cambridge, Cambridge, U.K., in 1991.

In 1991, he joined the University of New South Wales, Sydney, NSW, Australia, supported by an Australian Research Council Fellowship, before returning to the Cavendish Laboratory, University of Cambridge in 1995 as a Royal Society University Research Fellow, and subsequently Trevelyan Fellow of Selwyn College, Cambridge. Since 2002, he has been with the School of Electronic and Electrical Engineering, University of Leeds, as a Professor of electronic and photonic engineering, and is currently also the Pro-Dean for Research and Innovation with the Faculty of Engineering. His research interests include the optical and electronic properties of semiconductor devices, terahertz frequency electronics and photonics, and the exploitation of biological properties for nanostructure engineering.

Prof. Davies is a Fellow of the Royal Academy of Engineering and the Institute of Physics, and both a Chartered Physicist and Chartered Engineer. He received a Wolfson Research Merit award from the Royal Society in 2011, and shared the Faraday Medal and Prize from the Institute of Physics in 2014.

Nuria Llombart (S'06–M'07–SM'13) received the master's degree in electrical engineering and the Ph.D. degree from the Polytechnic University of Valencia, Valencia, Spain, in 2002 and 2006, respectively.

During her master's degree studies, she spent one year with the Friedrich-Alexander University of Erlangen-Nuremberg, Erlangen, Germany, and was with the Fraunhofer Institute for Integrated Circuits, Erlangen. From 2002 to 2007, she was with the Antenna Group, TNO Defense, Security and Safety, The Hague, The Netherlands, as a Ph.D. student and then as a Researcher. From 2007 to 2010, she was a Postdoctoral Fellow with the California Institute of Technology, Pasadena, CA, USA, where she was with the Submillimeter Wave Advance Technology Group, Jet Propulsion Laboratory. She was a "Ramón y Cajal" Fellow with the Optics Department, Complutense University of Madrid, Madrid, Spain, from 2010 to 2012. In 2012, she joined the THz Sensing Group, Technical University of Delft, Delft, The Netherlands, where she is currently a Full Professor. She has co-authored more than 150 journal and international conference contributions. Her current research interests include the analysis and design of planar antennas, periodic structures, reflector antennas, lens antennas, and waveguide structures, with emphasis in the terahertz range.

Dr. Llombart was the recipient of the H. A. Wheeler Award for the Best Applications Paper of 2008 in the IEEE TRANSACTIONS ON ANTENNAS AND PROPAGATION, the 2014 THz Science and Technology Best Paper Award of the IEEE Microwave Theory and Techniques Society, several NASA awards, and the 2014 IEEE Antenna and Propagation Society Lot Shafai Mid-Career Distinguished Achievement Award. In 2015, she was the recipient of European Research Council Starting Grant. She serves as a Board Member of the IRMMW-THz International Society.

Andrea Neto (M'00–SM'10–F'16) received the Laurea degree (summa cum laude) in electronic engineering from the University of Florence, Florence, Italy, in 1994, and the Ph.D. degree in electromagnetics from the University of Siena, Siena, Italy, in 2000. Part of his Ph.D. degree was developed at the European Space Agency Research and Technology Center Noordwijk, The Netherlands.

He was with the Antenna Section, European Space Agency Research and Technology Center for over two years. From 2000 to 2001, he was a Postdoctoral Researcher with the California Institute of Technology, Pasadena, CA, USA, where he was with the Submillimeter-Wave Advanced Technology Group. From 2002 to 2010, he was a Senior Antenna Scientist with TNO Defense, Security and Safety, The Hague, The Netherlands. In 2010, he became a Full Professor of applied electromagnetism with the EEMCS Department, Technical University of Delft, Delft, The Netherlands, where he formed and leads the Terahertz Sensing Group. His current research interests include the analysis and design of antennas with an emphasis on arrays, dielectric lens antennas, wideband antennas, EBG structures, and terahertz antennas.

Dr. Neto served as an Associate Editor of the IEEE TRANSACTIONS ON ANTENNAS AND PROPAGATION from 2008 to 2013 and the IEEE ANTENNAS AND WIRELESS PROPAGATION LETTERS from 2005 to 2013. He is a member of the Technical Board of the European School of Antennas and an organizer of the course on antenna imaging techniques. He is a member of the Steering Committee of the Network of Excellence NEWFOCUS, dedicated to focusing techniques in millimeter and submilliemeter-wave regimes. In 2011, he was a recipient of the European Research Council Starting Grant to perform research on Advanced Antenna Architectures for THz Sensing Systems, the H. A. Wheeler Award for the best applications paper of 2008 in the IEEE TRANSACTIONS ON ANTENNAS AND PROPAGATION, the Best Innovative Paper Prize of the 30th ESA Antenna Workshop in 2008, the Best Antenna Theory Paper Prize of the European Conference on Antennas and Propagation (EuCAP) in 2010.